CHEMICAL PHYSICS

Electric field–induced selective catalysis of single-molecule reaction

Xiaoyan Huang[1]*, Chun Tang[1]*, Jieqiong Li[1]*, Li-Chuan Chen[1,2]*, Jueting Zheng[1], Pei Zhang[1], Jiabo Le[1], Ruihao Li[1], Xiaohui Li[1], Junyang Liu[1]†, Yang Yang[1], Jia Shi[1], Zhaobin Chen[1], Mindong Bai[3], Hao-Li Zhang[2], Haiping Xia[1], Jun Cheng[1]†, Zhong-Qun Tian[1], Wenjing Hong[1]†

Oriented external electric fields (OEEFs) offer a unique chance to tune catalytic selectivity by orienting the alignment of the electric field along the axis of the activated bond for a specific chemical reaction; however, they remain a key experimental challenge. Here, we experimentally and theoretically investigated the OEEF-induced selective catalysis in a two-step cascade reaction of the Diels-Alder addition followed by an aromatization process. Characterized by the mechanically controllable break junction (MCBJ) technique in the nanogap and confirmed by nuclear magnetic resonance (NMR) in bottles, OEEFs are found to selectively catalyze the aromatization reaction by one order of magnitude owing to the alignment of the electric field on the reaction axis. Meanwhile, the Diels-Alder reaction remained unchanged since its reaction axis is orthogonal to the electric fields. This orientation-selective catalytic effect of OEEFs reveals that chemical reactions can be selectively manipulated through the elegant alignment between the electric fields and the reaction axis.

INTRODUCTION

Monitoring and controlling reactivity and selectivity of chemical reactions at the single-molecule scale are a long-standing goal and challenge in chemistry (*1*–*3*). Recently, oriented external electric fields (OEEFs) have been found to provide such an efficient control (*4*–*7*) by reorganizing the electron distribution of molecules when subjected to electric fields and in stabilizing them into charge-separated resonance forms, thus electrostatically catalyzing the chemical reactions. OEEFs have been theoretically investigated (*4*, *8*–*13*) and experimentally proved to facilitate the Diels-Alder addition (*14*), bond cleavage of alkoxyamine (*15*) and acetyl group (*16*), spin crossover molecular switch (*17*), carbon nanotube growth (*18*), and the activation of C1 compounds such as methane (*19*) or carbon dioxide (*20*). Nevertheless, the question of how to orient the direction of electric fields to align the energy on the chemical bond and reaction axis, achieving activation of a specific chemical reaction (*4*) and even enantioselectivity and stereoselectivity (*6*, *13*), currently remains as theoretical predictions.

To explore the role of OEEFs in selective electrostatic catalysis, two major challenges remain: one is the applied highly oriented and intensive electric fields to target molecules and the other is the characterization technique to investigate the reactions at the single-molecule level. For the first challenge, the electric field needs to be high enough (10^7 to 10^9 V/m) to trigger the charge separation with a large dipole moment (*5*). What is more, flipping the polarization of the field leads to the acceleration or inhibition of chemical reactions (*14*), even different species of product emerge (*8*, *9*, *18*). Further theoretical predictions also suggested that enantioselectivity and stereoselectivity can be achieved by applying an electric field in different directions (*6*, *13*), thus enabling the syntheses of pure enantiomers without further purification. For the second challenge, single-molecule electronics adopt nanoelectrodes to capture and investigate charge transport properties at the single-molecule scale (*21*–*23*), providing opportunities to apply an intense electric field with almost the same scale mentioned above on a single molecule. Recent advances in scanning tunneling microscope break junction (STM-BJ) (*14*, *24*–*26*) and mechanically controllable break junction (MCBJ) (*27*–*30*) methods demonstrated the detections of the reactant and product during the chemical reactions (*29*, *31*). Moreover, even the kinetics of chemical reactions at the single-molecule scale could be quantitatively extracted (*29*, *32*–*34*). Therefore, by controlling the relative orientation between electric fields and the reaction axis of individual molecules bridged within the nanogaps, the selective reaction acceleration of OEEFs could be investigated.

Here, we investigate the selective electrostatic catalysis of OEEFs in different processes of a cascade reaction by tuning the relative orientation between OEEFs and the reaction axis at the single-molecule scale using the MCBJ method. A two-step cascade reaction at room temperature was selected, where compound **a** [3,6-di(4-pyridyl)-1,2,4,5-tetrazine] undergoes an inverse electron demand Diels-Alder (iEDDA) reaction with dihydrofuran to form **b** (*35*–*37*), and a subsequent aromatization reaction occurs to form **c** (Fig. 1A and left column of Fig. 1B) (*38*–*40*). The reaction axis of the Diels-Alder reaction (**a**→**b**) is orthogonal to the direction of OEEFs, while the subsequent aromatization process (**b**→**c**) presents a nonorthogonal configuration between the reaction axis and OEEFs (Fig. 1A, top panel), which offers a test bed for the evaluation of the electric field–induced selective catalysis of chemical reactions. The reaction kinetics of this cascade reaction are determined from simultaneous single-molecule conductance monitoring using the MCBJ technique and parallel nuclear magnetic resonance (NMR) measurements, and the role of OEEFs in the electric field–induced catalysis is further revealed by combined density functional theory (DFT) calculations.

---

[1] State Key Laboratory of Physical Chemistry of Solid Surfaces, *i*ChEM (Collaborative Innovation Center of Chemistry for Energy Materials), National Engineering Laboratory for Green Chemical Productions of Alcohols-Ethers-Esters, College of Chemistry and Chemical Engineering, Xiamen University, Xiamen 361005, China. [2] State Key Laboratory of Applied Organic Chemistry, College of Chemistry and Chemical Engineering, Lanzhou University, Lanzhou 730000, China. [3] College of the Environment and Ecology, Xiamen University, Xiamen 361005, China.
*These authors contributed equally to this work.
†Corresponding author. Email: jyliu@xmu.edu.cn (J. Liu); chengjun@xmu.edu.cn (J.C.); whong@xmu.edu.cn (W.H.)

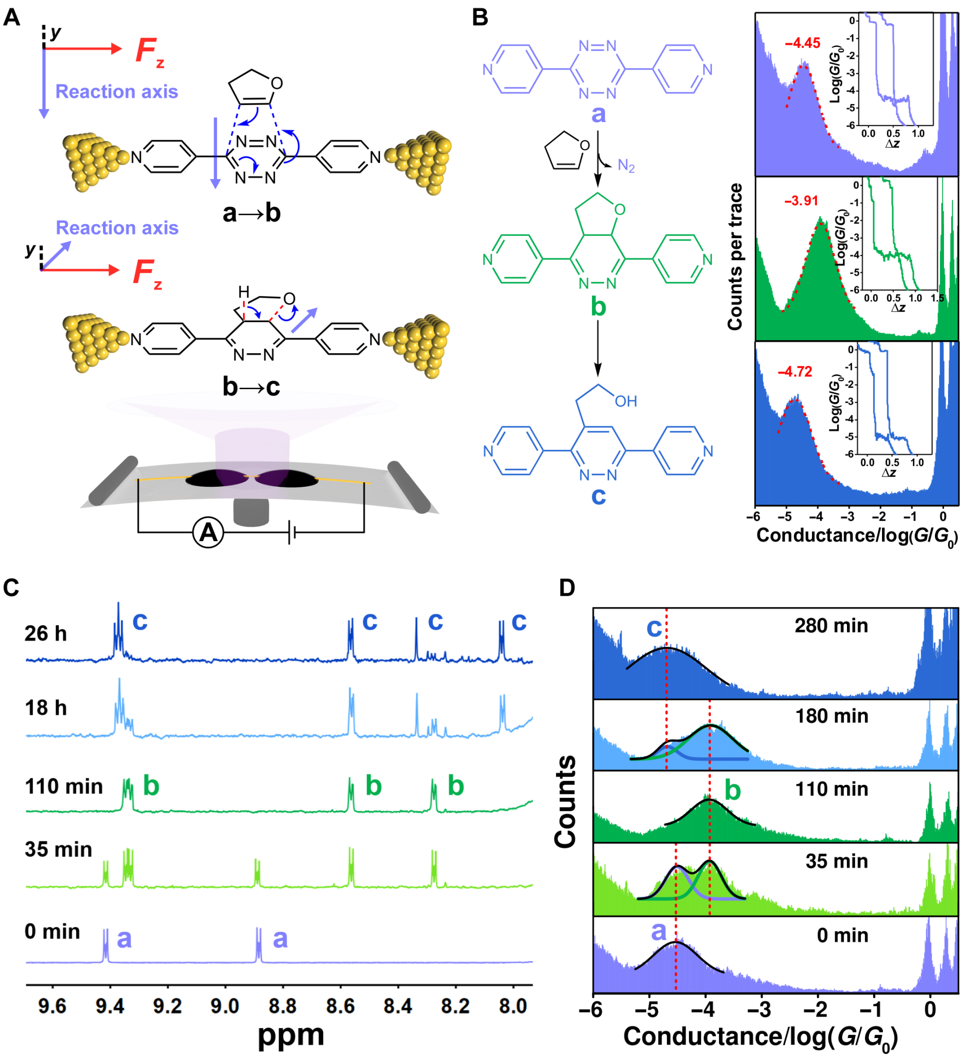

Fig. 1. Reaction investigation using single-molecule charge transport measurement and simultaneous NMR characterization. (**A**) Schematic of the MCBJ technique for in situ single-molecule conductance measurement. The Diels-Alder reaction axis (blue arrow) is orthogonal to the direction of electric field F_z (red arrow) and parallel to the *y* axis, while the reaction axis of the subsequent aromatization is proposed to be nonorthogonal to the electric field. (**B**) The left column shows the Diels-Alder reaction between 3,6-di(4-pyridyl)-1,2,4,5-tetrazine (**a**) and 2,3-dihydrofuran to form compound **b**, which goes through an aromatization process to form compound **c**. The single-molecule conductance of each compound was characterized in the right column through conductance histograms: **a** at $10^{-4.45}$ G_0, **b** at $10^{-3.91}$ G_0, and **c** at $10^{-4.72}$ G_0 (purple for **a**, green for **b**, and blue for **c**). Each histogram was constructed from 3000 individual conductance-distance traces, with typical traces shown in the inset of each panel. Monitoring the complete transformation from **a** to **c** through ^{1}H NMR (**C**) for 26 hours and conductance (**D**) for 4.7 hours. Each conductance histogram was constructed from approximately 300 conductance-distance traces that were collected in 5-min intervals, and the histograms were analyzed by Gaussian fitting to determine the area ratio between different components. The dashed lines represent the conductance value of each compound.

RESULTS

Reaction investigation using single-molecule conductance measurement and NMR

To better investigate the reaction kinetics, after selection of the appropriate solvent and concentration, we carried out the MCBJ experiment (Fig. 1A) in a mixed solvent of dichloromethane (DCM) and mesitylene (TMB) (1:4, v/v). From a solution with 1 mM concentration of **a**, a prominent peak at $10^{-4.45}$ G_0 (where G_0 is the conductance quantum, which equals to $2e^2/h$) was observed in the conductance histogram (Fig. 1B, top right) constructed from 3000 individual conductance-distance traces (for typical traces presenting a clear plateau, see the inset). Then, 1 M 2,3-dihydrofuran solution was added to the solution of **a** to form compound **b**. The corresponding conductance histogram (Fig. 1B, middle right) of **b**, which was also constructed from 3000 individual conductance-distance traces (see typical traces in the inset), suggesting that the conductance of **b** ($10^{-3.91}$ G_0) was distinguishably higher than that of **a**. Then, another peak occurred at a lower conductance (180 min in Fig. 1D), suggesting the isomerization of compound **b** to aromatic product **c**, and the peak of **c** was dominant and centered at $10^{-4.72}$ G_0 (280 min in Fig. 1D, which can be confirmed in the bottom right panel of Fig. 1B through the measurement of pure compound **c**). This trend in conductance, **b** > **a** > **c**, is in analogy to previous experimental and theoretical results, where the molecular structure with the least aromaticity mostly prefers the formation of a quinoidal structure with the smallest stabilization energy (*23*, *41*–*43*) to better couple the gold electrode and the central cyclic unit, thus causing the highest conductance. This trend also agrees with the charge transport calculation (see the “Structure-conductivity relationships” section in the Supplementary Materials). Additional two-dimensional (2D) conductance histograms (fig. S5, H and I) demonstrated that all the molecular structures during the whole reaction process show almost the same plateau length distributions, suggesting that the reaction only took place on the central ring, while the molecular backbone remained rigid, indicating that the conductance changes originate from the structural changes in the central core resulting from the chemical reaction.

To compare this process in single-molecule junctions and in the NMR tube, we performed in situ ^{1}H NMR characterization in parallel under the same conditions (for better comparison, deuterated DCM was used in both conductance and NMR measurements). The NMR spectra shown in Fig. 1C (fig. S3A) indicate that this iEDDA reaction took place at room temperature to produce compound **b** (*36*, *38*) on the same time scale as the reaction during the conductance measurements, which is also confirmed by the synchronous ultraviolet-visible (UV-vis) adsorption spectra (fig. S2). The complete conversion to compound **c**, however, took more than 26 hours, which was much slower than the reaction in single-molecule junctions. Subsequently, more detailed spectroscopic characterizations of the final product were carried out and confirmed the generation of compound **c** (see fig. S1 and the “Characterization data” section in the Supplementary Materials) (*38*, *44*). In Fig. 1D, which shows the single-molecule conductance evolution observed on the same time scale as the NMR measurements, each histogram was constructed from approximately 300 traces recorded every 5 min (fig. S6E). In agreement with the NMR results, we observed that the conductance peak separation during the conversion from **a** to **b** occurred on the same time scale, and both techniques suggested that it took approximately 110 min to complete the Diels-Alder addition. However, the conversion from **b** to **c** revealed by conductance measurements was complete at 280 min, which was notably faster than that characterized from NMR analysis, suggesting that the aromatization reaction was selectively accelerated under the single-molecule conductance measurement conditions.

Reaction kinetics of the two-step cascade reaction

To quantitatively determine the reaction kinetics under both conditions, the proportion of each component at each time scale was calculated through peak area integration of the conductance histograms (see Fig. 1D and the “In situ single-molecule conductance monitoring during the reaction” section in the Supplementary Materials) and NMR spectra (see Fig. 1C and the “Kinetic information extracted from the in situ ^{1}H NMR spectra” section in the Supplementary Materials), as summarized in Fig. 2 (A and B) (solid circles for conductance and hollow circles for NMR) (*29*, *32*, *33*). Therefore, the reaction rates of this process for both measurements were fitted (in Fig. 2, A and B, the solid line denotes the conductance measurement and the dashed line denotes the NMR measurement). During the first stage, the reaction rate constant k in the conductance measurement is 3.59×10^{-2} mM min^{-1}, which is comparable to the k' value obtained from the NMR measurement (see Fig. 2A and the “Reaction kinetics of conductance measurements under different bias voltages” section in the Supplementary Materials). In contrast, during the second stage, the fitted k value of 6.31×10^{-3} mM min^{-1} in the conductance measurement is approximately 10-fold larger than the k' value of 6.92×10^{-4} mM min^{-1} (see Fig. 2B and the “Reaction kinetics of conductance measurements under different bias voltages” section in the Supplementary Materials). Therefore, the extracted quantitative reaction kinetics demonstrate a significant selective reaction acceleration effect of OEEFs on the aromatization.

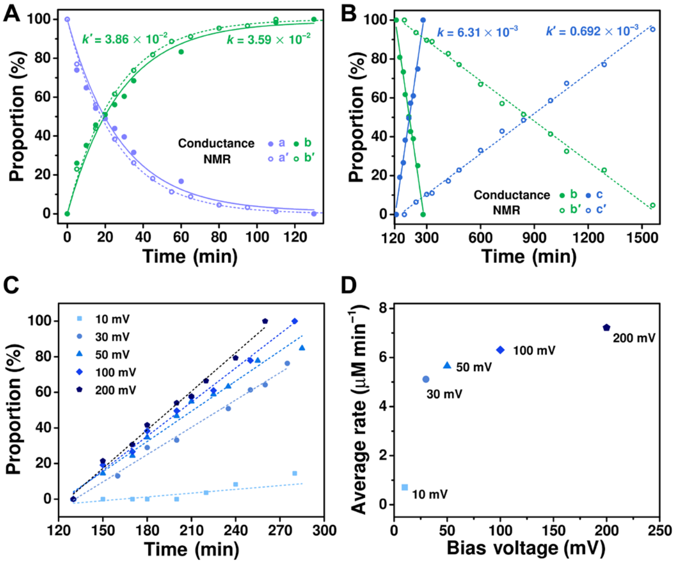

Fig. 2. Reaction kinetics in single-molecule junctions with OEEFs and in NMR tube. The relative proportion between different components analyzed from in situ single-molecule conductance measurement and NMR analysis for (**A**) the Diels-Alder addition process and (**B**) the aromatization process in this cascade reaction. The hollow circles and solid circles represent the results analyzed from NMR and conductance histograms, respectively. The data points were fitted with dashed and solid lines, respectively. (**C**) Reaction kinetics of the aromatization process in single-molecule junctions under different bias voltages. The proportion of compound **c** was also extracted from conductance histograms. The square represents the reaction under 10 mV; solid circle, 30 mV; triangle, 50 mV; diamond, 100 mV; and pentagon, 200 mV. (**D**) The reaction rate for the transformation from compound **b** to **c** varies under different bias voltages according to the fitted results in (C).

To further confirm the selective catalytic effect of OEEFs, we carried out conductance measurements under different bias voltages to reveal the magnitude of the field intensity dependence of the reaction. When the bias voltage was set to 10, 30, 50, or 200 mV, the Diels-Alder reaction still processed completely within 110 min (see the “Reaction kinetics of conductance measurements under different bias voltages” section in the Supplementary Materials). In contrast, as the bias voltage increased, the subsequent aromatization was significantly accelerated, as presented in Fig. 2C and summarized in Fig. 2D, increasing k_{10} to 0.71×10^{-3} mM min^{-1}, k_{30} to 5.11×10^{-3} mM min^{-1}, k_{50} to 5.65×10^{-3} mM min^{-1}, k_{100} to 6.31×10^{-3} mM min^{-1}, and k_{200} to 7.22×10^{-3} mM min^{-1}. These results indicate a field intensity dependence of the reaction rate, which strongly suggests that the increased electric field selectively facilitates the aromatization reaction instead of the Diels-Alder addition.

Catalytic selectivity mechanisms through the external electric fields

DFT calculations were carried out to probe the role of OEEFs in the reaction selectivity. In the first process of Diels-Alder reaction, the reaction barrier changes little with the applied OEEFs (see the blue curve in Fig. 3A and fig. S9, A and B), which is consistent with the orthogonal orientation between the reaction axis of the Diels-Alder

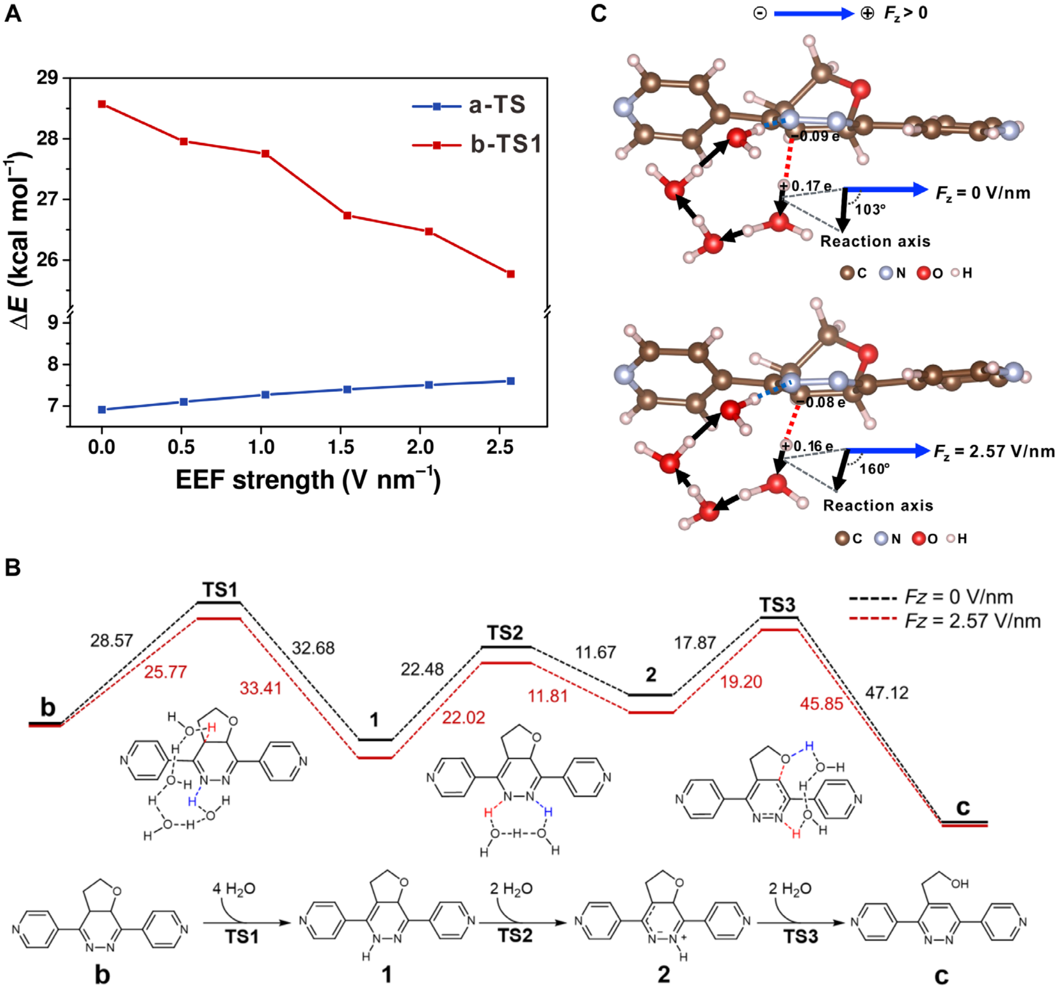

Fig. 3. Theoretical investigation of OEEF-induced selective reaction acceleration. (**A**) Reaction barriers (kcal/mol) of **a**→**TS** and **b**→**TS1** in DCM/TMB mixed solution under various OEEF strength along the *z* direction ($F_z > 0$, where *z* is oriented along the N—N bond of compound **a** and the positive direction of the OEEF is defined from the negative charge to the positive charge). (**B**) Energy profiles of reaction **b**→**c** with OEEFs ($F_z = 0.005$ a.u., where 1 a.u. = 514 V/nm; red lines) and without OEEFs (black lines). For **b**→**c**, the energetically optimum route is a three-step mechanism via water molecule–assisted proton relay. Among these three steps, the 1,3-hydrogen migration to the closest N atom to form more stable dihydropyridazine **1** (energy barriers of 28.57 kcal/mol without OEEFs and 25.77 kcal/mol with $F_z = 0.005$ a.u.) is the key step. (**C**) The blue arrow shows the positive direction of F_z. The bottom panels represent the configurations of **TS1** at $F_z = 0$ V/nm and $F_z = 2.57$ V/nm, respectively, which has a nonorthogonal reaction axis to F_z with a 103° and 160° angle. The red and blue dotted lines represent the bond cleavage and formation, respectively. The applied OEEFs favor the positively charged H atom leaving, which leads to C—H bond cleavage.

process and the direction of OEEFs. This finding highlights the importance of the relative orientation between the reaction axis and OEEFs, in which a parallel arrangement shows the catalytic activity of OEEFs (*6*, *14*).

To understand the significantly accelerated aromatization process from **b** to **c**, we evaluated several reaction pathways. We found that the involvement of water molecules is the most favorable, while other mechanisms without water molecules are difficult to continue. This may be attributed to that when proton transfer is mediated by water molecules acting as a bridge of proton relay, the space distance of the proton directly shifting to the next site is shortened and the strain in the transition state (TS) is reduced, resulting in a lower reaction barrier in the electric field catalysis (see the "Calculation of reaction pathways" section in the Supplementary Materials). This mechanism was also confirmed by control experiments involving acid or base, both of which inhibited aromatization (fig. S4), indicating that the trace amounts of water present in the solvent play an important role in the aromatization process. The most energetically favorable route for the transformation from **b** to **c** goes through two intermediates (see Fig. 3B and the "Calculation of reaction pathways" section in the Supplementary Materials), and the water-assisted 1,3-hydrogen migration (*45*) shows much stronger sensitivity with the presence of an oriented electric field (see the reaction barriers in red relative to the ones without OEEFs in black in Fig. 3B). A decrease of ~2.8 kcal/mol in the barrier (28.57 kcal/mol at $F_z = 0$ V/nm and 25.77 kcal/mol at $F_z = 2.57$ V/nm) from the theoretical simulation is quantitatively consistent with the experimentally evaluated data (~1.3 kcal/mol) derived from the rate constant difference in the **b**→**c** reaction (*k* of 6.92×10^{-4} mM min^{-1} from the NMR measurement and *k* of 6.31×10^{-3} mM min^{-1} from the conductance measurement) according to the Arrhenius equation (see the "Calculation of reaction barrier difference from experimental data" section in the Supplementary

Materials). The reduced energy barrier under OEEFs may arise from the favorable orientation of the TS versus the oriented OEEFs, which has also been proposed in other theoretical work (*12*). The reaction axis for the formation of intermediate **TS1** shows a nonorthogonal orientation to OEEFs along the *z* direction (Fig. 3C, bottom panels), and the angle between the C—H cleavage direction and F_z increases from 103° (at $F_z = 0$ V/nm) to 160° (at $F_z = 2.57$ V/nm). According to the positive charge population of the migrated H atom in **TS1** (Fig. 3C), it is intuitive that the positively charged H atom that moves along the negative direction of the above oriented component of the electric fields is facilitated by OEEFs with a 160° orientation. It is also consistent with the result that increasing F_z leads to shorter C—H distance in **TS1** (fig. S10D); thus, the reaction barriers decrease. What is more, it is found that the *z* dipole moment of **TS1** becomes more negative than that of the corresponding reactant under various positive OEEFs (fig. S10B). Thus, the **TS1**, with stronger dipole moment, shows a much more intense interaction with electric field than that of reactant **b**, leading to a smaller barrier.

DISCUSSION

To conclude, we investigated the role of OEEFs in the selective electrostatic catalysis in different processes of a cascade tetrazine Diels-Alder addition and the subsequent aromatization. By comparing the chemical kinetics characterized using in situ NMR in the bulk phase and charge transport investigations at the single-molecule scale, the aromatization process was found to be nonorthogonal to OEEFs in single-molecule junctions. This rate was nearly an order of magnitude faster than in the bulk phase. However, the reaction kinetics of the Diels-Alder reaction, which was orthogonal to OEEFs, were confirmed to be similar in both techniques. This selective catalytic effect is verified through theoretical simulation, which shows that the applied external electric field, when oriented favorably against the reaction coordinate, can stabilize the TS and reduce the reaction barrier of the aromatization process. Our results demonstrate that an external electric field could offer a new opportunity to tune the reaction rates and selectivity of chemical reactions for efficient chemical synthesis and even green chemistry in the future.

MATERIALS AND METHODS

Synthesis and NMR

All the chemicals, reagents, and solvents from commercial sources were used as received without further purification unless otherwise noted. The synthesis of product **c** is provided in the "Materials and synthetic methods" section of the Supplementary Materials. ^{1}H and ^{13}C NMR spectra were recorded with a Bruker AVIII-500 spectrometer (500 and 125 MHz, respectively) or a Bruker AVIII-850 spectrometer at 298 K (850 and 213 MHz, respectively). The spectra were referenced to residual proton-solvent references (^{1}H: CD_2Cl_2, 5.32 ppm; ^{13}C: CD_2Cl_2, 53.84 ppm). High-resolution mass spectra were recorded with a Bruker En Apex Ultra 7.0T FT-MS mass spectrometer. Synthesis and NMR characterization are provided in fig. S1.

Conductance measurements

The single-molecule conductance measurements were performed using the MCBJ technique with a homebuilt MCBJ setup at room temperature, as described in previous reports (*29*, *31*). For further details, see the "Conductance measurements by MCBJ technique" section in the Supplementary Materials. To carry out the conductance measurement, the solution contained 1 mM target molecules in the mixture solvent of deuterated DCM:TMB (1:4, v/v). A blank experiment of solvent without the target molecule is presented in fig. S5 (C to E).

Reaction kinetics from conductance and NMR measurements

The in situ electrical and NMR characterizations proceeded at the same time scale during the reaction. In addition, using the same concentration of the reagents in the same DCM/TMB solution, the mixed solution was separated into two parts: one for ^{1}H NMR characterizations and the other for conductance monitoring (both of these measurements started after the reaction occurred). The single-molecule conductance evolution was observed as the reaction time increased, and each histogram was constructed with about 300 traces recorded from each set of data. The 1D conductance histograms were fitted by Gaussian function with peak differentiation, and the corresponding peak areas were integrated to determine the proportions of each specific molecular species. Thus, we could determine the proportion of the products at each time scale for further reaction rate evaluation. For further details, see the "In situ single-molecule conductance monitoring during the reaction" section in the Supplementary Materials. For the NMR spectroscopies characterized at each time scale, the concentration ratio of product/reactant can also be derived from the area integration of the H peaks of each species. For further details, see the "Kinetic information extracted from the in situ ^{1}H NMR spectra" section in the Supplementary Materials.

DFT calculation

The molecular geometries and TSs were optimized by the Gaussian 09 program suite based on the DFT. The equilibrium geometries, including reactants, TSs, intermediates, and products, were optimized at the hybrid meta exchange-correlation M06-2X functional with 6-31+G(d) basis set. The vibrational frequencies were calculated at the same level to identify the stationary points and TSs with zero and one imaginary vibrational mode, respectively. TSs were also verified by both examination of the normal mode and the intrinsic reaction coordinate (IRC) calculations. To explore the influence of OEEFs on the activation barrier, various field strengths (E_F) from $E_F = -0.005$ to $E_F = +0.005$ a.u. (about ±2.57 V/nm) with 0.001 a.u. increments were applied. The static electric field was set along the *z* reaction axis, where *z* is oriented along the N—N bond of the reactants. For further details, see the "Computational setup" section in the Supplementary Materials. The theoretical transport properties were obtained by first-principles calculations (Atomistix ToolKit software package, ATK2013) using the combination of the DFT treatment for the electronic structure and the nonequilibrium Green's function (NEGF) formalism in simulation of coherent transport. A double-ζ plus polarization (DZP) basis set with a local density approximation was used for all atoms in the simulated device. All calculations used the polarizable continuum implicit solvation model (PCM) to account for the solvation effect of DCM/TMB mixed solution with a dielectric constant $\varepsilon = 3.598$. Further details are provided in the "Structure-conductivity relationships" section in the Supplementary Materials.

SUPPLEMENTARY MATERIALS

Supplementary material for this article is available at http://advances.sciencemag.org/cgi/content/full/5/6/eaaw3072/DC1

Section S1. Supplementary experimental methods

Section S2. Single-molecule charge transport by MCBJ technique

Section S3. Computational methods and results
Fig. S1. The characterization spectra of products **b** and **c**.
Fig. S2. The evolution of the UV-vis spectra for Diels-Alder reaction under the same condition with in situ NMR measurements.
Fig. S3. In situ ^{1}H NMR spectra evolution during the whole reaction.
Fig. S4. Control experiments to evaluate the effect of gold wire and the influences of acid and base.
Fig. S5. Single-molecule conductance measurements of **a**, **b**, and **c**.
Fig. S6. Reaction kinetics of single-molecule junctions under different bias voltages.
Fig. S7. Transmission calculations of **a**, **b**, and **c**.
Fig. S8. The reaction pathway evaluations of **b**→**c** in the absence of OEEFs.
Fig. S9. The calculated reaction barriers from **a** to **c** and versus the OEEF strengths.
Fig. S10. The free energies, *z* dipole moments, charge distributions, and bond distances of TSs under various OEEF strengths; more elaborate calculations of **b**→**1** versus small OEEF strengths.
Table S1. The energy barriers ($\Delta G^{\ddagger}_{\mathbf{b}\rightarrow \mathbf{TS1}}$, kcal/mol), free energy changes between **1** and **b** (ΔG, kcal/mol), and the entropy (kcal mol^{-1} K^{-1}) for each component in the absence of OEEFs.
References (*46*–*59*)

REFERENCES AND NOTES

1. Y. Jiang, Q. Huan, L. Fabris, G. C. Bazan, W. Ho, Submolecular control, spectroscopy and imaging of bond-selective chemistry in single functionalized molecules. *Nat. Chem.* **5**, 36–41 (2013).
2. K. Anggara, K. Huang, L. Leung, A. Chatterjee, F. Cheng, J. C. Polanyi, Bond selectivity in electron-induced reaction due to directed recoil on an anisotropic substrate. *Nat. Commun.* **7**, 13690 (2016).
3. A. Riss, A. P. Paz, S. Wickenburg, H.-Z. Tsai, D. G. De Oteyza, A. J. Bradley, M. M. Ugeda, P. Gorman, H. S. Jung, M. F. Crommie, A. Rubio, F. R. Fischer, Imaging single-molecule reaction intermediates stabilized by surface dissipation and entropy. *Nat. Chem.* **8**, 678–683 (2016).
4. S. Shaik, D. Mandal, R. Ramanan, Oriented electric fields as future smart reagents in chemistry. *Nat. Chem.* **8**, 1091–1098 (2016).
5. S. Ciampi, N. Darwish, H. M. Aitken, I. Díez-Pérez, M. L. Coote, Harnessing electrostatic catalysis in single molecule, electrochemical and chemical systems: A rapidly growing experimental tool box. *Chem. Soc. Rev.* **47**, 5146–5164 (2018).
6. S. Shaik, R. Ramanan, D. Danovich, D. Mandal, Structure and reactivity/selectivity control by oriented-external electric fields. *Chem. Soc. Rev.* **47**, 5125–5145 (2018).
7. F. Che, J. T. Gray, S. Ha, N. Kruse, S. L. Scott, J.-S. McEwen, Elucidating the roles of electric fields in catalysis: A perspective. *ACS Catal.* **8**, 5153–5174 (2018).
8. S. Shaik, S. P. de Visser, D. Kumar, External electric field will control the selectivity of enzymatic-like bond activations. *J. Am. Chem. Soc.* **126**, 11746–11749 (2004).
9. H. Hirao, H. Chen, M. A. Carvajal, Y. Wang, S. Shaik, Effect of external electric fields on the C–H bond activation reactivity of nonheme iron–oxo reagents. *J. Am. Chem. Soc.* **130**, 3319–3327 (2008).
10. G. A. Somorjai, J. Y. Park, Molecular factors of catalytic selectivity. *Angew. Chem. Int. Ed.* **47**, 9212–9228 (2008).
11. M. Akamatsu, N. Sakai, S. Matile, Electric-field-assisted anion–π catalysis. *J. Am. Chem. Soc.* **139**, 6558–6561 (2017).
12. R. Ramanan, D. Danovich, D. Mandal, S. Shaik, Catalysis of methyl transfer reactions by oriented external electric fields: Are gold–thiolate linkers innocent? *J. Am. Chem. Soc.* **140**, 4354–4362 (2018).
13. Z. Wang, D. Danovich, R. Ramanan, S. Shaik, Oriented-external electric fields create absolute enantioselectivity in Diels–Alder reactions: Importance of the molecular dipole moment. *J. Am. Chem. Soc.* **140**, 13350–13359 (2018).
14. A. C. Aragonès, N. L. Haworth, N. Darwish, S. Ciampi, N. J. Bloomfield, G. G. Wallace, I. Diez-Perez, M. L. Coote, Electrostatic catalysis of a Diels–Alder reaction. *Nature* **531**, 88–91 (2016).
15. L. Zhang, E. Laborda, N. Darwish, B. B. Noble, J. H. Tyrell, S. Pluczyk, A. P. Le Brun, G. G. Wallace, J. Gonzalez, M. L. Coote, S. Ciampi, Electrochemical and electrostatic cleavage of alkoxyamines. *J. Am. Chem. Soc.* **140**, 766–774 (2018).
16. M. Lindner, M. Valášek, M. Mayor, T. Frauhammer, W. Wulfhekel, L. Gerhard, Molecular graph paper. *Angew. Chem. Int. Ed.* **56**, 8290–8294 (2017).
17. G. D. Harzmann, R. Frisenda, H. S. J. van der Zant, M. Mayor, Single-molecule spin switch based on voltage-triggered distortion of the coordination sphere. *Angew. Chem. Int. Ed.* **54**, 13425–13430 (2015).
18. J. Wang, X. Jin, Z. Liu, G. Yu, Q. Ji, H. Wei, J. Zhang, K. Zhang, D. Li, Z. Yuan, J. Li, P. Liu, Y. Wu, Y. Wei, J. Wang, Q. Li, L. Zhang, J. Kong, S. Fan, K. Jiang, Growing highly pure semiconducting carbon nanotubes by electrotwisting the helicity. *Nat. Catal.* **1**, 326–331 (2018).
19. L. Yue, J. Li, S. Zhou, X. Sun, M. Schlangen, S. Shaik, H. Schwarz, Control of product distribution and mechanism by ligation and electric field in the thermal activation of methane. *Angew. Chem. Int. Ed.* **56**, 10219–10223 (2017).
20. M. Liu, Y. Pang, B. Zhang, P. De Luna, O. Voznyy, J. Xu, X. Zheng, C. T. Dinh, F. Fan, C. Cao, F. P. G. de Arquer, T. S. Safaei, A. Mepham, A. Klinkova, E. Kumacheva, T. Filleter, D. Sinton, S. O. Kelley, E. H. Sargent, Enhanced electrocatalytic CO_2 reduction via field-induced reagent concentration. *Nature* **537**, 382–386 (2016).
21. C. Huang, A. V. Rudnev, W. Hong, T. Wandlowski, Break junction under electrochemical gating: Testbed for single-molecule electronics. *Chem. Soc. Rev.* **44**, 889–901 (2015).
22. D. Xiang, X. Wang, C. Jia, T. Lee, X. Guo, Molecular-scale electronics: From concept to function. *Chem. Rev.* **116**, 4318–4440 (2016).
23. T. A. Su, M. Neupane, M. L. Steigerwald, L. Venkataraman, C. Nuckolls, Chemical principles of single-molecule electronics. *Nat. Rev. Mater.* **1**, 16002 (2016).
24. B. Xu, N. Tao, Measurement of single-molecule resistance by repeated formation of molecular junctions. *Science* **301**, 1221–1223 (2003).
25. L. Venkataraman, J. E. Klare, C. Nuckolls, M. S. Hybertsen, M. L. Steigerwald, Dependence of single-molecule junction conductance on molecular conformation. *Nature* **442**, 904–907 (2006).
26. M. H. Garner, H. Li, Y. Chen, T. A. Su, Z. Shangguan, D. W. Paley, T. Liu, F. Ng, H. Li, S. Xiao, C. Nuckolls, L. Venkataraman, G. C. Solomon, Comprehensive suppression of single-molecule conductance using destructive σ-interference. *Nature* **558**, 415–419 (2018).
27. R. Frisenda, V. A. E. C. Janssen, F. C. Grozema, H. S. J. van der Zant, N. Renaud, Mechanically controlled quantum interference in individual π-stacked dimers. *Nat. Chem.* **8**, 1099–1104 (2016).
28. F. Schwarz, G. Kastlunger, F. Lissel, C. Egler-Lucas, S. N. Semenov, K. Venkatesan, H. Berke, R. Stadler, E. Lörtscher, Field-induced conductance switching by charge-state alternation in organometallic single-molecule junctions. *Nat. Nanotechnol.* **11**, 170–176 (2016).
29. C. Huang, M. Jevric, A. Borges, S. T. Olsen, J. M. Hamill, J.-T. Zheng, Y. Yang, A. Rudnev, M. Baghernejad, P. Broekmann, A. U. Petersen, T. Wandlowski, K. V. Mikkelsen, G. C. Solomon, M. Brøndsted Nielsen, W. Hong, Single-molecule detection of dihydroazulene photo-thermal reaction using break junction technique. *Nat. Commun.* **8**, 15436 (2017).
30. O. S. Lumbroso, L. Simine, A. Nitzan, D. Segal, O. Tal, Electronic noise due to temperature differences in atomic-scale junctions. *Nature* **562**, 240–244 (2018).
31. J. Liu, X. Zhao, Q. Al-Galiby, X. Huang, J. Zheng, R. Li, C. Huang, Y. Yang, J. Shi, D. Z. Manrique, C. J. Lambert, M. R. Bryce, W. Hong, Radical enhanced charge transport in single-molecule phenothiazine electrical junctions. *Angew. Chem. Int. Ed.* **56**, 13061–13065 (2017).
32. L. Xiang, J. L. Palma, Y. Li, V. Mujica, M. A. Ratner, N. Tao, Gate-controlled conductance switching in DNA. *Nat. Commun.* **8**, 14471 (2017).
33. H. Wen, W. Li, J. Chen, G. He, L. Li, M. A. Olson, A. C. H. Sue, J. F. Stoddart, X. Guo, Complex formation dynamics in a single-molecule electronic device. *Sci. Adv.* **2**, e1601113 (2016).
34. J. Guan, C. Jia, Y. Li, Z. Liu, J. Wang, Z. Yang, C. Gu, D. Su, K. N. Houk, D. Zhang, X. Guo, Direct single-molecule dynamic detection of chemical reactions. *Sci. Adv.* **4**, eaar2177 (2018).
35. A.-C. Knall, C. Slugovc, Inverse electron demand Diels-Alder (iEDDA)-initiated conjugation: A (high) potential click chemistry scheme. *Chem. Soc. Rev.* **42**, 5131–5142 (2013).
36. B. S. Pilgrim, D. A. Roberts, T. G. Lohr, T. K. Ronson, J. R. Nitschke, Signal transduction in a covalent post-assembly modification cascade. *Nat. Chem.* **9**, 1276–1281 (2017).
37. F. Liu, R. S. Paton, S. Kim, Y. Liang, K. N. Houk, Diels–Alder reactivities of strained and unstrained cycloalkenes with normal and inverse-electron-demand dienes: Activation barriers and distortion/interaction analysis. *J. Am. Chem. Soc.* **135**, 15642–15649 (2013).
38. J. Sauer, D. K. Heldmann, J. Hetzenegger, J. Krauthan, H. Sichert, J. Schuster, 1,2,4,5-tetrazine: Synthesis and reactivity in [4+2] cycloadditions. *Eur. J. Org. Chem.* **1998**, 2885–2896 (1998).
39. J. Sauer, P. Bäuerlein, W. Ebenbeck, C. Gousetis, H. Sichert, T. Troll, F. Utz, U. Wallfahrer, [4+2] cycloadditions of 1,2,4,5-tetrazines and cyclopropenes - synthesis of 3,4-diazanorcaradienes and tetracyclic aliphatic azo compounds. *Eur. J. Org. Chem.* **2001**, 2629–2638 (2001).
40. M. L. Blackman, M. Royzen, J. M. Fox, Tetrazine ligation: Fast bioconjugation based on inverse-electron-demand Diels–Alder reactivity. *J. Am. Chem. Soc.* **130**, 13518–13519 (2008).
41. W. Chen, H. Li, J. R. Widawsky, C. Appayee, L. Venkataraman, R. Breslow, Aromaticity decreases single-molecule junction conductance. *J. Am. Chem. Soc.* **136**, 918–920 (2014).
42. A. Borges, G. C. Solomon, Effects of aromaticity and connectivity on the conductance of five-membered rings. *J. Phys. Chem. C* **121**, 8272–8279 (2017).
43. S. Fujii, S. Marqués-González, J.-Y. Shin, H. Shinokubo, T. Masuda, T. Nishino, N. P. Arasu, H. Vázquez, M. Kiguchi, Highly-conducting molecular circuits based on antiaromaticity. *Nat. Commun.* **8**, 15984 (2017).
44. L. R. Domingo, M. T. Picher, J. A. Sáez, Toward an understanding of the unexpected regioselective Hetero-Diels-Alder reactions of asymmetric tetrazines with electron-rich ethylenes: A DFT study. *J. Org. Chem.* **74**, 2726–2735 (2009).
45. B. F. Yates, L. Radom, Intramolecular hydrogen migration in ionized amines: A theoretical study of the gas-phase analogs of the Hofmann-Loeffler and related rearrangements. *J. Am. Chem. Soc.* **109**, 2910–2915 (1987).

46. W. Hong, H. Valkenier, G. Mészáros, D. Z. Manrique, A. Mishchenko, A. Putz, P. M. García, C. J. Lambert, J. C. Hummelen, T. Wandlowski, An MCBJ case study: The influence of π-conjugation on the single-molecule conductance at a solid/liquid interface. *Beilstein J. Nanotechnol.* **2**, 699–713 (2011).
47. W. Hong, D. Z. Manrique, P. Moreno-García, M. Gulcur, A. Mishchenko, C. J. Lambert, M. R. Bryce, T. Wandlowski, Single molecular conductance of tolanes: Experimental and theoretical study on the junction evolution dependent on the anchoring group. *J. Am. Chem. Soc.* **134**, 2292–2304 (2012).
48. V. D. Kiselev, E. A. Kashaeva, G. G. Iskhakova, M. Shihab, A. I. Konovalov, Volume, enthalpy and entropy of activation of the Diels-Alder reaction of dimethyl 1,2,4,5-tetrazine-3,6-dicarboxylate with 1-hexene. *Tetrahedron* **55**, 12201–12210 (1999).
49. D. Z. Manrique, C. Huang, M. Baghernejad, X. Zhao, O. A. Al-Owaedi, H. Sadeghi, V. Kaliginedi, W. Hong, M. Gulcur, T. Wandlowski, M. R. Bryce, C. J. Lambert, A quantum circuit rule for interference effects in single-molecule electrical junctions. *Nat. Commun.* **6**, 6389 (2015).
50. M. J. Frisch, G. W. Trucks, H. B. Schlegel, G. E. Scuseria, M. A. Robb, J. R. Cheeseman, *Gaussian 09, Revision d.01* (Gaussian Inc., 2009).
51. Y. Zhao, D. G. Truhlar, The M06 suite of density functionals for main group thermochemistry, thermochemical kinetics, noncovalent interactions, excited states, and transition elements: Two new functionals and systematic testing of four M06-class functionals and 12 other functionals. *Theor. Chem. Acc.* **120**, 215–241 (2008).
52. W. J. Hehre, R. Ditchfield, J. A. Pople, Self-consistent molecular orbital methods. XII. Further extensions of Gaussian-type basis sets for use in molecular orbital studies of organic molecules. *J. Chem. Phys.* **56**, 2257–2261 (1972).
53. M. J. Frisch, J. A. Pople, J. S. Binkley, Self-consistent molecular orbital methods 25. Supplementary functions for Gaussian basis sets. *J. Chem. Phys.* **80**, 3265–3269 (1984).
54. E. Cancès, B. Mennucci, J. Tomasi, A new integral equation formalism for the polarizable continuum model: Theoretical background and applications to isotropic and anisotropic dielectrics. *J. Chem. Phys.* **107**, 3032–3041 (1997).
55. M. Cossi, V. Barone, B. Mennucci, J. Tomasi, Ab initio study of ionic solutions by a polarizable continuum dielectric model. *Chem. Phys. Lett.* **286**, 253–260 (1998).
56. M. Brandbyge, J.-L. Mozos, P. Ordejón, J. Taylor, K. Stokbro, Density-functional method for nonequilibrium electron transport. *Phys. Rev. B* **65**, 165401 (2002).
57. J. Taylor, H. Guo, J. Wang, Ab initio modeling of quantum transport properties of molecular electronic devices. *Phys. Rev. B* **63**, 245407 (2001).
58. T. Lu, F. Chen, Atomic dipole moment corrected hirshfeld population method. *J. Theor. Comput. Chem.* **11**, 163–183 (2012).
59. S. V. Aradhya, M. Frei, M. S. Hybertsen, L. Venkataraman, Van der waals interactions at metal/organic interfaces at the single-molecule level. *Nat. Mater.* **11**, 872–876 (2012).

Acknowledgments: We thank Prof. Qing-Biao Li in Xiamen University for fruitful discussions. **Funding:** This work was supported by the National Key R&D Program of China (2017YFA0204902), the National Natural Science Foundation of China (21722305, 21703188, 21673195, 21621091, 51733004, 51525303, and 91745103), the China Postdoctoral Science Foundation (2017M622060), and the Young Thousand Talents Project of China. **Author contributions:** W.H. and J. Liu originally conceived the concept. J. Liu, J.C., and W.H. co-supervised the project. J. Liu, X.H., C.T., L.-C.C., J. Li, J.C., and W.H. prepared the manuscript using feedback from all authors. Break junction measurements and conductance data analyses were carried out by X.H., J. Liu, and J.Z. in W.H.'s group. MCBJ setup was constructed by R.L., J.S., and Z.C. in W.H.'s group. NMR experiments and corresponding data analyses were conducted by C.T. and P.Z. in H.X.'s group. Theoretical simulations were carried out by C.T., J. Li., and L.-C.C. in J.C., H.-L.Z. and W.H.'s groups. Y.Y., X.L., M.B., H.X., H.-L.Z., and Z.-Q.T. helped revise and polish the manuscript. All authors gave approval to the final version of the manuscript. **Competing interests:** The authors declare that they have no competing interests. **Data and materials availability:** All data needed to evaluate the conclusions in the paper are present in the paper and/or the Supplementary Materials. Additional data related to this paper may be requested from the authors.

Submitted 11 December 2018
Accepted 10 May 2019
Published 21 June 2019
10.1126/sciadv.aaw3072

Citation: X. Huang, C. Tang, J. Li, L.-C. Chen, J. Zheng, P. Zhang, J. Le, R. Li, X. Li, J. Liu, Y. Yang, J. Shi, Z. Chen, M. Bai, H.-L. Zhang, H. Xia, J. Cheng, Z.-Q. Tian, W. Hong, Electric field–induced selective catalysis of single-molecule reaction. *Sci. Adv.* **5**, eaaw3072 (2019).